

Observation of the Direct Energy Band Gaps of Defect-Tolerant Cu<sub>3</sub>N by Ultrafast Pump-Probe Spectroscopy

Matthew Zervos,\* Andreas Othonos, Marios Sergides, Theodore Pavloulidis, and Joseph Kioseoglou

Cite This: *J. Phys. Chem. C* 2020, 124, 3459–3469

Read Online

ACCESS |

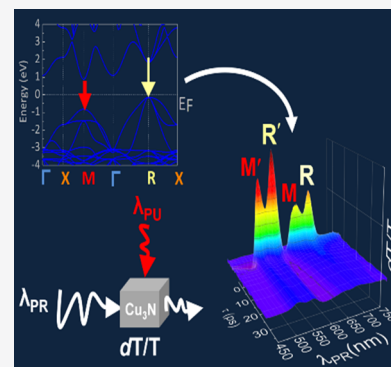


Metrics &amp; More



Article Recommendations

**ABSTRACT:** Cu<sub>3</sub>N with a cubic crystal structure has been prepared from Cu on fused SiO<sub>2</sub> under a flow of NH<sub>3</sub>:O<sub>2</sub> between 400 and 600 °C. All Cu<sub>3</sub>N layers exhibited distinct maxima in differential transmission at ~500, 550, and 630, 670 nm with the same spectral structure and shape on a ps timescale as shown by ultrafast pump-probe spectroscopy. We show that the maxima at 630 (≡1.97 eV) and 670 nm (≡1.85 eV) correspond to the M and R direct energy band gaps of Cu<sub>3</sub>N, in excellent agreement with density functional theory calculations of the electronic band structure. These findings are corroborated further by the fact that Cu<sub>3</sub>N as-deposited by reactive sputtering under 100% N<sub>2</sub> at 25 °C and 10<sup>-2</sup> mbar did not exhibit a fine spectral structure due to a smeared density of states, poor crystallinity, and a high density of defects, but annealing under NH<sub>3</sub>:H<sub>2</sub> at 300 °C revealed a similar spectral structure to Cu<sub>3</sub>N obtained from Cu under NH<sub>3</sub>:O<sub>2</sub>. In contrast to the above, we suggest that the peaks at 500 (≡2.48 eV) and 550 nm (≡2.25 eV) might correspond to the M and R direct gaps of certain regions of Cu<sub>3</sub>N under strain that changes the lattice constant and band gap. We discuss the charge carrier generation and recombination mechanisms in terms of Cu interstitials and vacancies that are known to be energetically located near the band edges, thus allowing the observation of the direct energy band gaps in this defect tolerant semiconductor.



## 1. INTRODUCTION

Cu<sub>3</sub>N,<sup>1</sup> Zn<sub>3</sub>N<sub>2</sub>,<sup>2</sup> and Sn<sub>3</sub>N<sub>4</sub><sup>3</sup> are earth-abundant metal nitrides, which are interesting from fundamental and technological points of view, but Cu<sub>3</sub>N has been investigated in greater detail due to its unique properties that are attractive for energy conversion and storage. Cu<sub>3</sub>N has a cubic  $\alpha$ -ReO<sub>3</sub> crystal structure with a lattice constant of 3.8 Å and a space group of *Pm3m*, number 221, as shown by Juza and Hahn<sup>4</sup> as early as 1938. It is similar to the ABX<sub>3</sub> anti-perovskite structure with a vacant body-center position, so it can readily accommodate impurities and is a defect-tolerant semiconductor. This makes it attractive for solar cells,<sup>5</sup> batteries,<sup>6</sup> and catalysis.<sup>7</sup> In addition, it has been shown to be suitable not only for optical storage, as it can be transformed into Cu by heating above 300 °C,<sup>8,9</sup> but also for solid-state storage, as it exhibits resistive switching,<sup>10,11</sup> and finally for the realization of sensors.<sup>12</sup>

Cu<sub>3</sub>N has been obtained by a variety of methods including sputtering,<sup>6,3–37</sup> molecular beam epitaxy,<sup>38</sup> atomic layer deposition,<sup>39,40</sup> and pulsed laser deposition.<sup>41,42</sup> Recently, Matsuzaki et al.<sup>43</sup> have obtained Cu<sub>3</sub>N from Cu under NH<sub>3</sub> and O<sub>2</sub> between 500 and 800 °C. However, in the past, most have obtained Cu<sub>3</sub>N by sputtering of Cu under N<sub>2</sub> in conjunction with Ar, which enables control over its stoichiometry.

In general, Cu-rich Cu<sub>3</sub>N is n-type with a mobility of  $\mu_n = 0.1$  to 10 cm<sup>2</sup>/(V s) and carrier densities of  $n = 10^{16}$  to 10<sup>17</sup> cm<sup>-3</sup>,<sup>5,44</sup> while its resistivity has been shown to vary between  $\rho$

$= 10^{-2}$  to 10<sup>-5</sup> Ω cm.<sup>45</sup> In contrast, N-rich Cu<sub>3</sub>N is p-type, and its resistivity has been found to be larger and to vary between  $\rho = 10^{-1}$  and 10<sup>3</sup> Ω cm. Many efforts have also been devoted to doping and the incorporation of impurities into Cu<sub>3</sub>N. For example, Matsuzaki et al.<sup>43</sup> obtained p-type Cu<sub>3</sub>N via the incorporation of interstitial F, while Gao et al.<sup>46</sup> have shown that the incorporation of Zn resulted in n-type Cu<sub>3</sub>N and increased the carrier density from  $n = 10^{17}$  to 10<sup>21</sup> cm<sup>-3</sup> with a resistivity of 10<sup>-3</sup> Ω cm. It is also important to mention that Du et al.<sup>47,48</sup> found that the incorporation of O<sub>2</sub> increased the resistivity of Cu<sub>3</sub>N.

From the above, it is evident that one may tune the electrical properties of Cu<sub>3</sub>N by controlling the stoichiometry and/or by adding impurities. However, this also has a direct impact on the optical properties and energy band gap of Cu<sub>3</sub>N, which is strongly dependent on its lattice constant. All estimates of the optical energy band gap determined previously from steady-state UV–vis absorption-transmission spectroscopy,<sup>49–53</sup> UV–vis reflectance-transmission,<sup>54</sup> and spectroscopic ellipsometry<sup>23,55,56</sup> fall in the range of 1.2 to 2.4 eV. A single value for the optical band gap was determined in each case, but it was

Received: November 2, 2019

Revised: January 22, 2020

Published: January 23, 2020



not clarified if this corresponds to the direct or indirect energy bandgap. Only Sahoo et al.<sup>53</sup> claimed that the indirect and direct band gaps determined from steady-state UV–vis spectroscopy fall in the ranges of 1.17–1.68 and 1.72–2.38 eV, respectively, by changing the pressure during deposition, but the optical properties were not really understood previously in terms of the electronic band structure of Cu<sub>3</sub>N.

In contrast, Birkett et al.<sup>57</sup> investigated in detail the variation of the energy band gap with temperature using Fourier transform infrared spectroscopy in conjunction with theoretical calculations of the electronic band structure. In particular, they prepared Cu<sub>3</sub>N by sputtering under Ar and N<sub>2</sub>, and the direct energy band gap was found to be 1.68 eV at 300 K, but this changed only very slightly up to 1.7 eV at 4.2 K. This is consistent with the calculations of Birkett et al.,<sup>57</sup> who showed that the direct and indirect energy band gaps change slightly between 1.56 and 1.6 eV and 0.9 and 1.0 eV, respectively, between absolute zero and room temperature. More importantly, Birkett et al.<sup>57</sup> showed theoretically that the direct and indirect band gaps changed significantly from 1.4 to 2.0 eV and 0.6 to 1.8 eV, respectively, upon increasing the lattice constant from 3.8 to 3.9 Å that could occur under strain. Consequently, Cu<sub>3</sub>N is a defect-tolerant semiconductor in which one can readily incorporate impurities and accommodate structural distortion, but this has an immediate effect on the values of the direct and indirect band gaps and by extension on the optical properties. A detailed understanding of the optical properties in terms of the electronic band structure as well as the role of defects is therefore imperative. Such insight has been provided by Yee et al.,<sup>58</sup> who investigated the properties of N-rich Cu<sub>3</sub>N and confirmed the existence of Cu interstitials (Cu<sub>i</sub>) by photothermal deflection spectroscopy, which is an indirect method with dramatically higher sensitivity than UV–vis spectroscopy that can be used for the detection of sub-band gap states that are related to crystal imperfections and/or impurities. More specifically, Yee et al.<sup>58</sup> showed theoretically that the dominant intrinsic point defects are copper vacancies V<sub>(Cu)</sub>, which act as shallow acceptors, while copper interstitials Cu<sub>(i)</sub> behave as deep potential wells in the conduction band. This is in effect what makes Cu<sub>3</sub>N a defect-tolerant semiconductor, which is the tendency of a semiconductor to keep its properties despite the presence of crystallographic defects as pointed out by Zakutayev et al.<sup>5</sup> Consequently, Cu<sub>3</sub>N has shallow intrinsic defects and surface states, in contrast to the case of other nitrides such as GaN.

In the past, we have shown that sub-band gap states can also be detected by ultrafast pump-probe spectroscopy (UPPS). This method is also a sensitive technique and an effective tool for understanding the generation-recombination mechanisms and pathways of photoexcited electron-holes that depend on the electronic band structure and energetic position of states related to crystal imperfections and impurities.<sup>59,60</sup> To the best of our knowledge, no one has considered previously the properties of Cu<sub>3</sub>N by UPPS.

Consequently, we have carried out a detailed investigation into the fundamental properties of Cu<sub>3</sub>N by UPPS where the Cu<sub>3</sub>N was prepared from Cu on fused SiO<sub>2</sub> under a flow of NH<sub>3</sub>:O<sub>2</sub> between 300 and 600 °C, similar to Matsuzaki et al.<sup>43</sup> For comparison, we also prepared Cu<sub>3</sub>N by reactive sputtering on fused SiO<sub>2</sub> under 100% N<sub>2</sub> at 10<sup>−2</sup> mbar, which was subsequently annealed under NH<sub>3</sub>:H<sub>2</sub> between 300 and 400 °C. We find that we are able to detect clearly the M and R

direct band gaps of Cu<sub>3</sub>N by UPPS, in excellent agreement with theory because it is in essence a defect-tolerant semiconductor confirming that the defect states are indeed energetically located very close to the conduction and valence bands. This suggests that UPPS can be used as an effective tool for understanding Cu<sub>3</sub>N at a fundamental level, for example, finding how the direct energy band gap changes with strain, reduced dimensionality, and size, which in turn will provide deeper insight as to how it may be used for the realization of energy conversion devices such as solar cells.

## 2. EXPERIMENTAL SECTION

Initially, square samples of 10 mm × 10 mm fused SiO<sub>2</sub> (f-SiO<sub>2</sub>) with a thickness of ~1 mm and soda lime glass (SLG) were cleaned sequentially in trichloroethylene, methanol, acetone, and isopropanol after which they were rinsed in deionized water and dried with nitrogen. Subsequently, 30, 60, and 140 nm of Cu were deposited on the f-SiO<sub>2</sub> and SLG by sputtering of a Cu target using Ar at 10<sup>−2</sup> mbar. The conversion of Cu into Cu<sub>3</sub>N was carried out in a 1" chemical vapor deposition (CVD) reactor capable of reaching 1100 °C that was fed on the upstream side by a manifold consisting of four mass flow controllers connected to Ar, NH<sub>3</sub>, O<sub>2</sub>, and H<sub>2</sub>. The Cu on f-SiO<sub>2</sub> and SLG was loaded in a quartz boat that was inserted into the reactor after which it was purged with 1000 sccm Ar for 10 min at 1 bar. Then the temperature was ramped at 30 °C/min under a flow of 300 sccm NH<sub>3</sub> containing 15 sccm O<sub>2</sub>. Upon reaching the desired temperature, the same flow of NH<sub>3</sub> and O<sub>2</sub> was maintained for a further 30 min after which cool down took place over 10 min. The samples were removed only at room temperature after purging with a flow of 1000 sccm Ar for 10 min. The temperature of nitridation was varied between 400 and 600 °C, and besides NH<sub>3</sub>:O<sub>2</sub>, we also used just NH<sub>3</sub> and NH<sub>3</sub>:H<sub>2</sub> keeping all else equal.

In addition to the above, we have deposited Cu<sub>3</sub>N directly on f-SiO<sub>2</sub> by reactive sputtering of a Cu target under 100% N<sub>2</sub> at 10<sup>−2</sup> mbar. In this case, the substrate was not heated, but the layers were annealed afterward between 300 and 400 °C under NH<sub>3</sub>:H<sub>2</sub> in order to improve their crystal quality.

The morphology and crystal structure of the Cu<sub>3</sub>N were determined by scanning electron microscopy (SEM) and X-ray diffraction (XRD), while the optical properties of the resultant Cu<sub>3</sub>N on f-SiO<sub>2</sub> were investigated by steady-state UV–vis absorption transmission spectroscopy using a PerkinElmer spectrophotometer. More importantly, the time evolution of the differential transmission (dT/T) on a ps timescale was measured by UPPS using a pump of λ<sub>PU</sub> = 400 nm and probe λ<sub>PR</sub> that was varied between 450 and 750 nm as described in detail elsewhere.<sup>59</sup> The photoluminescence (PL) was measured at room temperature, and the excitation energy was the same as that used in the UPPS measurements, that is, 1 mJ/cm<sup>2</sup>, in order to prevent the decomposition of the material. The carrier density, mobility, and the resistivity were determined in the Van der Pauw configuration by the Hall effect using Ag contacts and a Keithley 2635A constant current source together with a Keithley 2182 voltmeter.

## 3. RESULTS AND DISCUSSION

**3.1. Structural Properties of Cu<sub>3</sub>N.** Cu is a transition metal with a face-centered cubic (fcc) crystal structure and a lattice constant of 3.597 Å. The deposition of 200 nm Cu by

sputtering on f-SiO<sub>2</sub> at room temperature resulted in the formation of a highly reflective film with metallic conductivity, but as expected, this exhibited only a few, very weak peaks in the XRD corresponding to the fcc crystal structure of Cu. We did not detect any peaks related to CuO or Cu<sub>2</sub>O, but this does not mean that the surface of Cu will not react with O<sub>2</sub> and H<sub>2</sub>O under ambient conditions and undergo oxidation. It has been shown by Platzman et al.<sup>61</sup> that the oxidation of Cu deposited by thermal evaporation involves three main stages: (a) the formation of a Cu<sub>2</sub>O layer, (b) the formation of metastable Cu(OH)<sub>2</sub> due to the reaction of Cu with OH<sup>−</sup> groups, and (c) the transformation of the Cu(OH)<sub>2</sub> to CuO. All of these three stages occur simultaneously and are mutually dependent on each other. However, before describing the conversion of Cu into Cu<sub>3</sub>N under NH<sub>3</sub>:O<sub>2</sub>, it is important to point out that the crystallinity of the 200 nm Cu layers was improved significantly by annealing under inert conditions, that is, Ar:10% H<sub>2</sub> at 10<sup>−1</sup> mbar. More specifically, all layers annealed between 400 and 600 °C maintained their metallic-like conductivity and exhibited improved crystallinity and stronger, well-resolved peaks in the XRD, corresponding to the fcc crystal structure of Cu. However, a significant diffusion of Cu into the underlying f-SiO<sub>2</sub> occurred above 600 °C. More specifically, we observed a total loss of the metallic conductivity at 700, 800, and 900 °C attributed to the diffusion of Cu into the f-SiO<sub>2</sub> and the out-diffusion of oxygen from the underlying f-SiO<sub>2</sub> into the Cu, not the evaporation of Cu, which has a melting point of 1085 °C. It should be noted that the diffusion of Cu deposited on SLG and the accompanying loss of metallic conductivity occurred at an even lower temperature of 600 °C, which is close to the melting point of glass. The same effect was observed by annealing 200 nm Cu deposited on sapphire, that is, Al<sub>2</sub>O<sub>3</sub>, above 700 °C despite the fact that Al<sub>2</sub>O<sub>3</sub> is considered to be a good barrier against the diffusion of Cu. Our observations are consistent with those of Rha et al.,<sup>62</sup> who showed that annealing Cu between 350 and 500 °C leads to the formation of larger grain sizes and reduces the resistivity of Cu, but temperatures in excess of 500 °C, that is, 550 °C, resulted in higher resistivity due to out-diffusion from the underlying substrate. Similarly, Lee et al.<sup>63</sup> obtained optimum conductivity and crystal quality at 400 °C.

Considering the constraint imposed by the diffusion of Cu into the f-SiO<sub>2</sub> and Al<sub>2</sub>O<sub>3</sub> and the out-diffusion of oxygen from the f-SiO<sub>2</sub> and Al<sub>2</sub>O<sub>3</sub> into the Cu, we converted a 200 nm Cu layer that was deposited by sputtering on f-SiO<sub>2</sub> into Cu<sub>3</sub>N under a flow of NH<sub>3</sub>:O<sub>2</sub> between 400 and 600 °C, similar to Matsuzaki et al.,<sup>43</sup> who deposited 200 nm Cu on glass by electron beam evaporation and converted this to Cu<sub>3</sub>N between 400 and 800 °C under NH<sub>3</sub>:O<sub>2</sub>. We observed a change in the color of Cu from highly reflective light-brown to gray and then gray-black by increasing the temperature from 300 to 600 °C, similar to the observations of Matsuzaki et al.<sup>43</sup> All of the Cu<sub>3</sub>N layers obtained this way exhibited strong and well-resolved peaks in the XRD as shown in Figure 1a belonging to the  $\alpha$ -ReO<sub>3</sub> cubic crystal structure of Cu<sub>3</sub>N. It is important to emphasize that we detected a peak at  $2\theta = 23.7^\circ$  corresponding to the (001) crystallographic plane of Cu<sub>3</sub>N that was observed by Matsuzaki et al.<sup>43</sup> from Cu<sub>3</sub>N grown on SrTiO<sub>3</sub> by molecular beam epitaxy after annealing under NH<sub>3</sub>. In addition, we also observe a peak at  $2\theta = 47.96^\circ$  corresponding to the (002) crystallographic plane of Cu<sub>3</sub>N, that is, the multiple of (001), which leads us to suggest that the

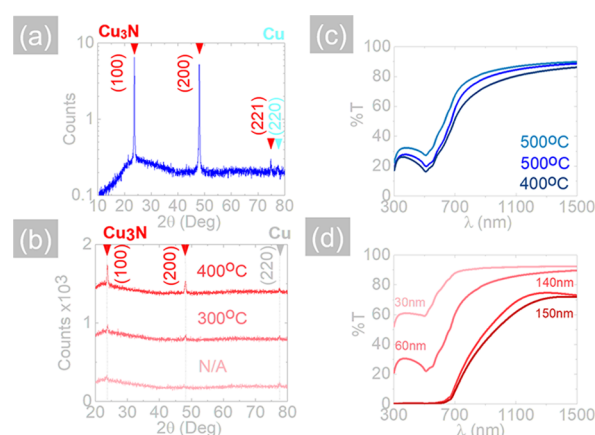


**Figure 1.** (a) XRD of Cu<sub>3</sub>N obtained from 200 nm Cu after annealing under NH<sub>3</sub>:O<sub>2</sub> at 600 °C (Max.  $2\theta$ : 23.7, 47.96, and 74.8° cf. cubic Cu<sub>3</sub>N  $2\theta$ : 23.3(100), 47.65(200), and 74.6°(221)); (b) XRD of 60 nm Cu<sub>3</sub>N as-deposited on f-SiO<sub>2</sub> by sputtering under 100% N<sub>2</sub> at 10<sup>−2</sup> mbar/25 °C, that is, not annealed (N/A) (Max.  $2\theta$ : = 23.54, 47.76, and 77.4°) and annealed under NH<sub>3</sub>:H<sub>2</sub> at 300 (Max.  $2\theta$ : 23.86, 48.18, and 77.58°) and 400 °C (Max.  $2\theta$ : 23.72, 48.11, and 77.52°); (c) optical transmission through 30 nm Cu<sub>3</sub>N obtained after annealing Cu on f-SiO<sub>2</sub> at 400 and 500 °C under NH<sub>3</sub>:O<sub>2</sub>; the trace at the top corresponds to Cu<sub>3</sub>N obtained from 30 nm Cu under NH<sub>3</sub>:H<sub>2</sub> at 500 °C; (d) optical transmission through 30, 60, and 140 nm Cu<sub>3</sub>N deposited on f-SiO<sub>2</sub> by sputtering and annealed under NH<sub>3</sub>:H<sub>2</sub> at 500 °C for 30 min.

Cu<sub>3</sub>N has crystallized in a very specific way and must consist of ordered and oriented crystals. Finally, we also observe a minor peak at  $2\theta = 74.8^\circ$  corresponding to the (221) crystallographic plane of Cu<sub>3</sub>N. Consequently, we observe a conversion of Cu into Cu<sub>3</sub>N, which occurs via a two-step reaction of Cu with O<sub>2</sub> and then with NH<sub>3</sub> as described by Matsuzaki et al.<sup>43</sup> In a way, it is similar to the conversion of metal oxides such as Ga<sub>2</sub>O<sub>3</sub> into GaN under NH<sub>3</sub>:H<sub>2</sub> at elevated temperatures.<sup>64</sup> It should be noted here that we also obtained Cu<sub>3</sub>N from Cu using just NH<sub>3</sub> as well as NH<sub>3</sub>:H<sub>2</sub>, which is in contrast to the findings of Matsuzaki et al.,<sup>43</sup> who showed that the Cu was not converted into Cu<sub>3</sub>N under NH<sub>3</sub>. We did not observe other XRD peaks related to CuO or Cu<sub>2</sub>O, in agreement with Matsuzaki et al.<sup>43</sup> despite the fact that the conversion of Cu into Cu<sub>3</sub>N was carried out under NH<sub>3</sub>:O<sub>2</sub> at temperatures well above 300 °C. However, we find that our Cu<sub>3</sub>N films consist of 76 at. % Cu, 23 at. % N, and contain some oxygen, that is, 2 at. % O, by energy-dispersive X-ray (EDX) analysis, but it is difficult to provide accurate estimates of the light elements using EDX. It should be emphasized also that the Cu<sub>3</sub>N layers do not bear an epitaxial relationship to the underlying substrate, so we expect any strain in the layers to arise from surface oxidation and/or the out-diffusion of oxygen from the substrate.<sup>87</sup> Upon closer consideration of the XRD peaks in Figure 1a, we find that the (001) peak at  $2\theta = 23.7^\circ$  is actually shifted by +0.4° with respect to the bulk at  $2\theta = 23.3^\circ$  (ID#86-2283, cubic Cu<sub>3</sub>N *Pm3m*, Number 221) for the 200 nm as well as the 30 nm Cu<sub>3</sub>N films on f-SiO<sub>2</sub>, which translates into a strain of ~2%. This has a strong effect on the M and R direct energy band gaps of Cu<sub>3</sub>N as shown in Figure 2d. All other peaks are very close to the bulk, unstrained peaks of Cu<sub>3</sub>N irrespective of thickness. Therefore, it appears that certain regions of the Cu<sub>3</sub>N layer will be strained and others will be not.

Before considering the optical properties of the Cu<sub>3</sub>N layers, we ought to mention that we also tried to prepare 30, 60, and



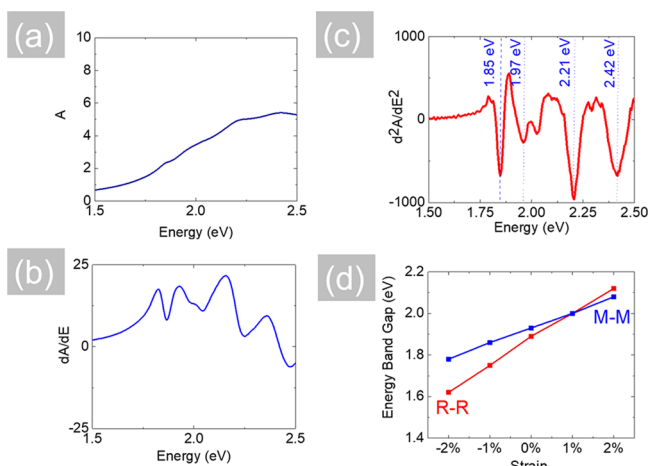


**Figure 2.** (a) Absorption of 30 nm  $\text{Cu}_3\text{N}$  annealing under  $\text{NH}_3:\text{O}_2$  at 400 °C; (b) first derivative of  $A$ , that is,  $dA/dE$  versus photon energy  $E$ ; (c) second derivative of  $A$ , that is,  $d^2A/dE^2$  versus photon energy  $E$  showing the energies of the local minima; (d) variation of the M and R direct energy band gaps with strain.

140 nm layers of  $\text{Cu}_3\text{N}$  directly on  $\text{f-SiO}_2$  held at room temperature by reactive sputtering of a Cu target using 99.999%  $\text{N}_2$  at  $10^{-2}$  mbar, which gives in essence N-rich growth conditions. These are very similar to the conditions used by Yee et al.,<sup>58</sup> who deposited  $\text{Cu}_3\text{N}$  on SLG and obtained  $p = 10^{17} \text{ cm}^{-3}$  and a hole mobility of  $2.65 \text{ cm}^2/(\text{V s})$ . The layers obtained in this way did not exhibit strong peaks in the XRD as shown in Figure 1b suggesting that the layers are largely amorphous but they contain crystalline domains of  $\text{Cu}_3\text{N}$  given that the first two XRD peaks are very close to those shown in Figure 1a. However, the peak in Figure 1b at  $2\theta = 77.5^\circ$  is indexed to (220) Cu as we observed the very same peak from a pure Cu layer that was deposited on  $\text{f-SiO}_2$ . The layers obtained in this way by reactive sputtering had a resistivity of  $\rho = 6.25 \text{ k}\Omega \text{ cm}$ , hole density of  $p = 2 \times 10^{16} \text{ cm}^{-3}$ , and a poor hole mobility of  $\mu_p = 0.05 \text{ cm}^2/(\text{V s})$ . We subsequently annealed them under  $\text{NH}_3:10\% \text{ H}_2$  for 30 min at 300 and 400 °C in order to improve the crystalline quality and reduce the density of defects, but we did not observe a great improvement in the intensity of the XRD peaks as shown in Figure 1b.

In order to investigate the properties of  $\text{Cu}_3\text{N}$  by steady-state and time-resolved optical spectroscopy, we deposited Cu on  $\text{f-SiO}_2$  and converted them into  $\text{Cu}_3\text{N}$  under  $\text{NH}_3:\text{O}_2$  as described above. The steady-state transmission spectra through 30 nm  $\text{Cu}_3\text{N}$  obtained from Cu at 400 and 500 °C under  $\text{NH}_3:\text{O}_2$  are shown in Figure 1c; the trace from  $\text{Cu}_3\text{N}$  obtained under  $\text{NH}_3:\text{H}_2$  at 500 °C is also shown for comparison. In addition, the steady-state UV–vis transmission through  $\text{Cu}_3\text{N}$  with different thicknesses obtained on  $\text{f-SiO}_2$  by reactive sputtering and annealing is shown in Figure 1d from which it is clear that a reduction in transparency occurs with increasing thickness. A critical point analysis of the steady-state UV–vis spectra obtained from the 30 nm  $\text{Cu}_3\text{N}$  was carried out in order to obtain the energies at which the absorption shows maxima using the derivative method. The absorption  $A$  versus photon energy is shown in Figure 2a, while the first derivative of the absorbance with respect to energy ( $dA/dE$ ) reveals critical points in absorption at its turning points as shown in Figure 2b. To precisely acquire where the absorbance obtains maximum values, the second derivative can be calculated to

acquire the transition energies at the minima. As shown in Figure 2c, the energy values obtained by this method are 1.85, 1.97, 2.21, and 2.42 eV. However, in order to understand what these energies correspond to, we have carried out UPSS and density functional theory (DFT) electronic structure calculations.

**3.2. Ultrafast Pump-Probe Spectroscopy.** All of the  $\text{Cu}_3\text{N}$  layers obtained from Cu on  $\text{f-SiO}_2$  under  $\text{NH}_3:\text{O}_2$  between 400 and 600 °C exhibited distinct maxima in differential transmission ( $dT/T_0$ ) versus probe wavelength ( $\lambda_{\text{PR}}$ ) at  $\sim 500$ , 550, 630, and 670 nm as shown in Figure 3a–d,

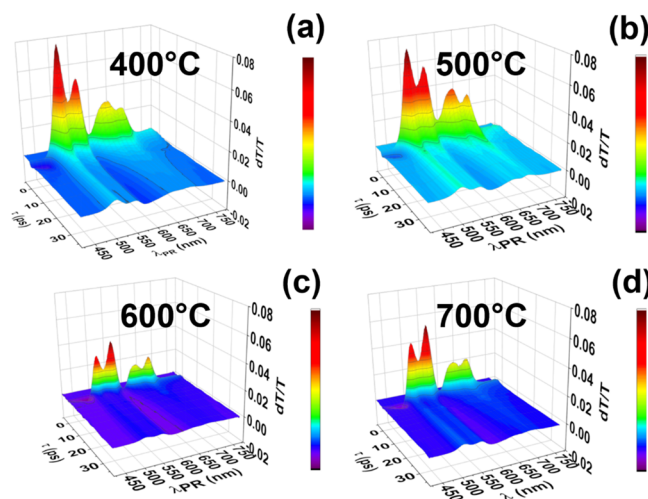


**Figure 3.** UPSS showing the time evolution of the differential transmission  $dT/T$  on a ps timescale versus  $\lambda_{\text{PR}}$  from  $\text{Cu}_3\text{N}$  obtained after annealing 30 nm Cu under  $\text{NH}_3:\text{O}_2$  for 30 min at (a) 400 °C (maxima at  $\lambda_{\text{PR}} = 503, 546, 627$ , and  $662 \text{ nm}$ ), (b) 500 °C (maxima at  $\lambda_{\text{PR}} = 503, 548, 626$ , and  $667 \text{ nm}$ ), (c) 600 °C (maxima at  $\lambda_{\text{PR}} = 507, 552, 630$ , and  $667 \text{ nm}$ ), and (d) 700 °C (maxima at  $\lambda_{\text{PR}} = 507, 552, 625, 665 \text{ nm}$ ).

which also depict their time evolution on a ps timescale. For clarity, differential transmission is defined as the change in transmission  $dT = T - T_0$  induced by the pump divided by the transmission  $T_0$  of the probe in the absence of the pump, that is,  $dT/T_0 = (T - T_0)/T_0$ . The exact  $\lambda_{\text{PR}}$ 's at which the maxima occur in each case are listed in Figure 3. For clarity, the differential transmission  $dT/T$  versus  $\lambda_{\text{PR}}$  at various instants of time delay for the  $\text{Cu}_3\text{N}$  obtained at 400 °C is shown in Figure 4a. The time evolution and decay of  $dT/T$  at  $\lambda_{\text{PR}} = 503, 546, 627$ , and  $662 \text{ nm}$  are shown in Figure 4b–e, respectively, and correspond to the maxima shown in Figure 4a. All traces follow a simple exponential decay, and the corresponding lifetimes were found to be 3.17, 3.43, 4.01, and 4.95 ps at  $\lambda_{\text{PR}} = 503, 546, 627$ , and  $662 \text{ nm}$ . Evidently, the lifetime increases with  $\lambda_{\text{PR}}$  as shown in Figure 4f. A similar trend was also obtained from  $\text{Cu}_3\text{N}$  obtained at 500, 600, and 700 °C, but the carrier lifetimes drop with increasing growth temperature.

All of the  $\text{Cu}_3\text{N}$  layers exhibited similar spectral structures and shapes as shown in Figure 3a–d, but this changed by increasing the intensity of excitation or energy of the pump from  $E = 0.1$  to  $2 \text{ mJ/cm}^2$  as shown in Figure 5a–d. However, the original spectral structure was obtained again and was identical to that shown in Figure 5a upon reducing the excitation energy from  $E = 2$  back to  $0.1 \text{ mJ/cm}^2$ . Consequently, the changes observed in Figure 5 are not

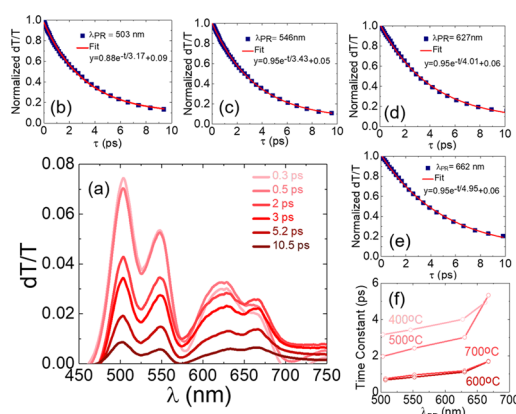


**Figure 4.** (a) Differential transmission  $dT/T$  versus  $\lambda_{PR}$  (nm) at various delays  $\tau$  (ps) through the  $\text{Cu}_3\text{N}$  obtained from 30 nm Cu under  $\text{NH}_3:\text{O}_2$  at 400 °C for 30 min. Also shown is the time evolution of the differential transmission  $dT/T$  on a ps timescale for (b)  $\lambda_{PR} = 503$  nm, (c)  $\lambda_{PR} = 546$  nm, (d)  $\lambda_{PR} = 627$  nm, and (e) 662 nm. The decays were fitted by a single exponential of the form  $y = Ae^{-t/\tau} + y_0$ , which was also observed for  $\text{Cu}_3\text{N}$  obtained at 500, 600, and 700 °C; (f) the time constants  $\tau$  (ps) versus  $\lambda_{PR}$  (nm) at the maxima for the different growth temperatures.

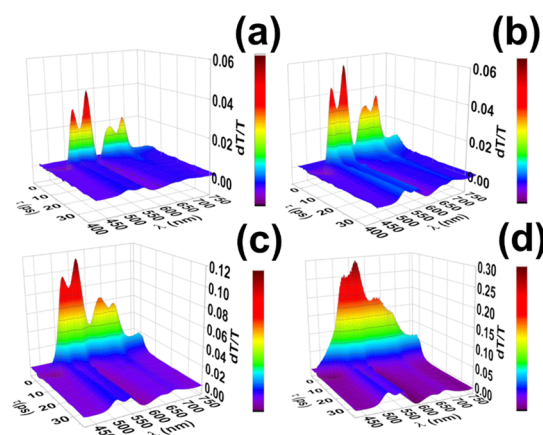


**Figure 5.** UPDS of  $\text{Cu}_3\text{N}$  obtained from 30 nm Cu on f- $\text{SiO}_2$  under  $\text{NH}_3:\text{O}_2$  for 30 min at 600 °C showing the time evolution of the differential transmission  $dT/T$  on a ps timescale versus  $\lambda_{PR}$  obtained under different excitation energies of (a) 0.1, (b) 0.2, (c) 0.5, and (d) 2  $\text{mJ}/\text{cm}^2$ .

related to any kinds of structural modifications or changes in the composition due to heating.

The temporal evolution of  $dT/T$  obtained by UPDS from the  $\text{Cu}_3\text{N}$  as-deposited by sputtering is shown for completeness in Figure 6a,b, which is very different from that of  $\text{Cu}_3\text{N}$  obtained from Cu under  $\text{NH}_3:\text{O}_2$  between 400 and 600 °C. However, we observed a finer spectral structure by UPDS after annealing as shown in Figure 6c,d. It is reasonable then to suggest that the spectral structure of the  $\text{Cu}_3\text{N}$  shown in Figure 6c,d is related to the formation of crystalline  $\text{Cu}_3\text{N}$  and a reduction in the density of defects. However, in order to understand the spectral structure shown in Figures 3 and 6, it is necessary to consider the electronic band structure of  $\text{Cu}_3\text{N}$  in detail as described next.

**3.3. Electronic Band Structure-Density Functional Theory Calculations.** Density functional theory (DFT) calculations were carried out using the Vienna ab initio Simulation Package (VASP)<sup>65,66</sup> with Projector Augmented-

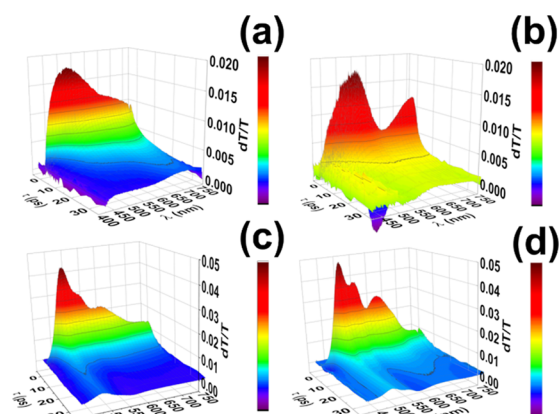


**Figure 6.** UPDS of (a) 30 and (b) 140 nm N-rich  $\text{Cu}_3\text{N}$  as-deposited by reactive sputtering on f- $\text{SiO}_2$  (c); (d) 30 nm N-rich  $\text{Cu}_3\text{N}$  obtained by reactive pattering on f- $\text{SiO}_2$  after annealing under  $\text{NH}_3:\text{H}_2$  for 30 min at 300 and 400 °C.

Wave (PAW) pseudopotentials.<sup>67,68</sup> The calculations were performed using Perdew–Burke–Ernzerhof Generalized Gradient Approximation (PBE-GGA)<sup>69,70</sup> functionals and range separated Heyd–Scuseria–Ernzerhof (HSE) hybrid functionals.<sup>71–73</sup> A mixing and screening parameter of  $\mu = 0.25$  and  $\alpha = 0.2$  were chosen, respectively, to select the HSE06 functional,<sup>74</sup> and the energy cutoff for the plane-wave basis set was 520 eV, while the tolerance for self-consistency was set at  $10^{-4}$  eV. In addition the pseudopotential used for Cu included 11 valence electrons in a  $3d^{10}4s^1$  configuration, while the pseudopotential used for N included five valence electrons in a  $2s^22p^3$  configuration. Moreover, a Gaussian with a smearing width of 0.01 eV was chosen for the partial occupancies of the electronic orbitals.

The Brillouin zone was sampled using a  $\Gamma$ -centered  $16 \times 16 \times 16$  mesh for the PBE-GGA and a  $\Gamma$ -centered  $8 \times 8 \times 8$  mesh for the HSE calculations of the four-atom cubic unit cell. Note that the DFT + U method was employed to properly describe the behavior of d electrons, which introduces a strong intra-atomic interaction in a screened Hartree–Fock-like manner that has been used in the past for transition-metal compounds.<sup>75,76</sup> More specifically, a simplified, rotationally invariant approach to DFT + U was used in accordance with Dudarev et al.<sup>77</sup> where the parameters  $U$  and  $J$  that control the effective on-site Coulomb interaction and on-site exchange interaction, respectively, are not entered separately and only the difference  $U_{\text{eff}} = U - J$  is meaningful; the +U potential was applied only to the d electrons of Cu.

We have calculated the electronic band structure of the energetically favorable structure of  $\text{Cu}_3\text{N}$ ,<sup>78,79</sup> that is, the  $\text{D0}_9$ , simple cubic structure of the anti- $\text{ReO}_3$  phase, with space group  $\text{Pm}\bar{3}\text{m}$  (No. 221).<sup>41,56,80</sup>  $U_{\text{eff}}$  is considered as a free parameter to be optimized and is scaled between  $U_{\text{eff}} = 0$  and 10. The lattice constants and band gaps of  $\text{Cu}_3\text{N}$  determined in this way are compared against the results obtained by hybrid functional calculations, which have been shown to reproduce accurately the lattice constants and band gaps of nitride semiconductors.<sup>81,82</sup>

A series of fixed volume relaxations was performed to determine the equilibrium lattice constants of  $\text{Cu}_3\text{N}$  for the respective  $U_{\text{eff}}$  value followed by the calculation of the electronic band structure and orbital-decomposed density of states (DOS).

The lattice constants and the band gaps vary almost linearly with  $U_{\text{eff}}$  as shown in Figure 7. A  $U_{\text{eff}}$  value of 2.61 eV

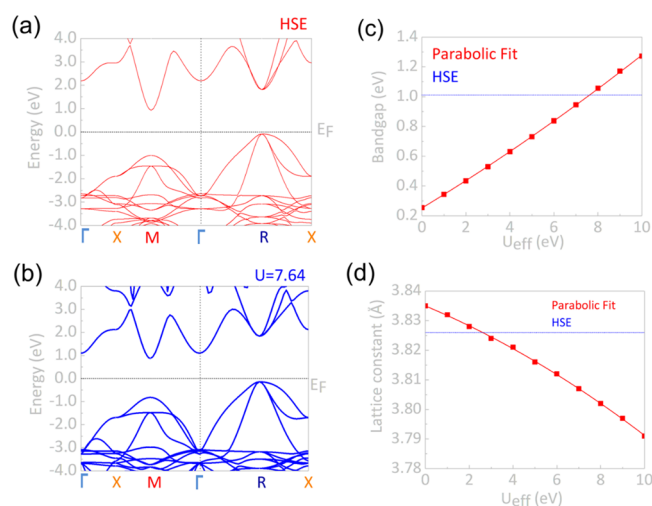


**Figure 7.** (a) Electronic band structure of Cu<sub>3</sub>N by HSE calculations; (b) electronic band structure of Cu<sub>3</sub>N with  $U_{\text{eff}} = 7.64$  eV; (c) variation of energy band gap versus  $U_{\text{eff}}$ ; (d) variation of lattice constant versus  $U_{\text{eff}}$ .

reproduces the lattice constant predicted by the HSE functionals, while a  $U_{\text{eff}}$  value of 7.64 eV reproduces the band gap predicted by the HSE functionals. This value is close to the optimized value of  $U_{\text{eff}} = 7$  eV for Cu<sub>2</sub>O.<sup>83</sup> The corresponding lattice constant is 3.804 Å. Hence, a  $U_{\text{eff}}$  value of 7.64 eV is also validated by the fact that the dominant experimentally measured lattice constants for stoichiometric Cu<sub>3</sub>N are found between 3.80 Å by Juza and Hahn<sup>4</sup> and 3.815 Å by recent studies of Gallardo-Vega and de la Cruz<sup>41</sup> and Zhao et al.<sup>80</sup> The electronic band structure is also shown in Figure 7. In both cases, the band gap is indirect with a valence band (VB) maximum at point R and a conduction band (CB) minimum at point M. By DFT+U the orbitals participating at the VB maximum are the N *p* orbitals with 10% contribution, Cu *s* orbitals with a 15% contribution, and Cu *d* orbitals with 75% contribution. The CB minimum is dominated by *p* orbitals with 65% contribution and *d* orbitals with 35% contribution of Cu atoms. These findings are in good agreement with electronic band structure calculations carried out previously on Cu<sub>3</sub>N.<sup>5,84–86</sup>

**3.4. Charge Carrier Generation and Recombination Mechanisms in Cu<sub>3</sub>N.** From the above, one may observe that the maxima at 627 (1.98 eV) and 662 nm (1.87 eV) shown in Figure 3 are very close to the M and R direct energy band gaps at 1.89 and 1.94 eV shown in Figure 8. Upon pumping and photoexcitation, electrons are initially promoted high into the conduction bands leaving holes in the valence band as shown in Figure 9a. The photoexcited electrons and holes will subsequently lose energy and occupy lower energy states that are empty in the M and R conduction bands resulting in state filling. The occupancy of states at a particular energy and state filling can be measured, that is, probed by the transmission or not of light with a wavelength of  $\lambda_{\text{PR}}$  that is varied between 450 and 750 nm. A state at certain energy that is occupied, that is, filled by a carrier, will result in the transmission of incident light with a wavelength of  $\lambda_{\text{PR}}$ , but if it is empty, then a photon will be absorbed promoting an electron into the empty state. In

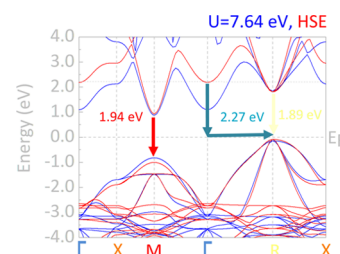


**Figure 8.** Electronic band structure of Cu<sub>3</sub>N showing the M and R direct band gap transitions observed experimentally but also the  $\Gamma$ –R indirect transition.

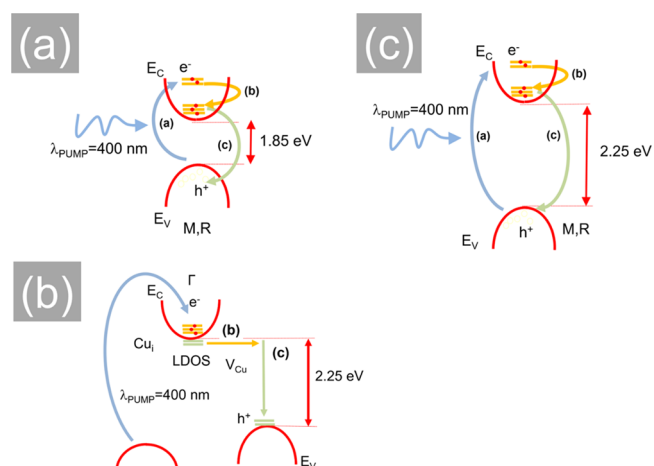


**Figure 9.** (a) M, R direct energy band gaps of Cu<sub>3</sub>N showing photoexcitation of electrons from the VB into empty states high in the CB, redistribution of electrons and state filling of lower energy states near the CB minimum, and recombination of electrons and holes; (b) schematic of the  $\Gamma$  and R valleys showing photoexcitation of electrons into empty states inside the CB and nonradiative recombination mediated by a local density of states (LDOS) of Cu<sub>(i)</sub> close to the CB minimum, which permits transitions to the R valley (c) as in panel (a) but the M and R direct energy band gaps of Cu<sub>3</sub>N are larger due to strain.

all cases, we observe the occurrence of state filling due to the positive differential transmission. We did not observe any free carrier excitation by the probe beam, that is, photons, with  $\lambda_{\text{PR}}$  in Cu<sub>3</sub>N following pumping that would result in a negative  $dT/T$  like we did previously in InN, which had a metallic-like conductivity and high carrier density of  $10^{20}$  cm<sup>−3</sup> resulting into a Fermi level that is energetically located above the conduction band minimum leading to the Burstein–Moss shift.<sup>59</sup>

Now, the maxima in the optical transmission at 627 (1.98 eV) and 662 nm (1.87 eV) shown in Figure 3 are straightforward to observe as they correspond to direct band gap transitions. To the best of our knowledge, no one has observed the direct energy band gaps of Cu<sub>3</sub>N in such a way previously. At this point, we ought to mention that the photogenerated electrons that occupy states in the M and R direct conduction bands and give rise to state filling do not recombine in a radiative fashion as Cu<sub>3</sub>N is fundamentally an indirect energy band gap semiconductor. This is corroborated by the fact that we did not detect any photoluminescence (PL) from the Cu<sub>3</sub>N between 77 and 300 K. Consequently, the photogenerated carriers must change momentum by interacting with impurities in order to undergo indirect transitions and



recombine in a nonradiative fashion. More specifically, during nonradiative, indirect transition recombination, an electron is first trapped by a defect and then one hole is captured leading to carrier recombination. In general, if the energetic position of the crystal imperfection is close to the conduction band minimum electrons will be easily trapped but not holes. Similarly, holes will be easily captured if the trap level is close to the valence band maximum but not electrons. Consequently, the recombination process is determined by a slower trapping rate for the electron or hole. Usually, midgap levels are invoked as being effective recombination centers in indirect band gap semiconductors. However, it has been shown that crystal imperfections in  $\text{Cu}_3\text{N}$  give rise to states that are energetically located close to or inside the conduction and valence bands.<sup>5,55,56</sup> In particular, Yee et al.<sup>58</sup> showed theoretically that the dominant intrinsic point defects copper vacancies  $V_{\text{Cu}}$  are shallow acceptors while copper interstitials  $\text{Cu}_{\text{i}}$  behave as deep potential wells in the conduction band. According to Yee et al.,<sup>58</sup>  $V_{\text{Cu}}$  and  $\text{Cu}_{\text{i}}$  have defect concentrations in the range of  $10^{14}$  to  $10^{17} \text{ cm}^{-3}$  for both Cu-poor and Cu-rich growth conditions and are the dominant intrinsic point defects giving rise to p-type and n-type conductivity, respectively. They confirmed the existence of  $\text{Cu}_{\text{i}}$  by photothermal deflection spectroscopy, which is an indirect absorption method with dramatically higher sensitivity than ultraviolet–visible spectroscopy (UV–vis) and can be used for the detection of sub-band gap defect states. Both  $\text{Cu}_{\text{i}}$  and  $V_{\text{Cu}}$  are capable of mediating Shockley–Read–Hall recombination and can absorb differences in momentum in this indirect band gap semiconductor, but the impurity states are not located in the forbidden energy, so even though they might be occupied by carriers, the  $\text{Cu}_3\text{N}$  appears to have a clear band gap as if it were defect-free. Defect tolerance then is the tendency of a semiconductor to keep its properties despite the presence of crystallographic defects as pointed out by Zakutayev et al.<sup>5</sup>

In short then, the photogeneration of electrons will populate states in the direct energy conduction bands, and subsequently, the carriers will undergo nonradiative recombination via indirect transitions in  $\text{Cu}_3\text{N}$  mediated by  $V_{\text{Cu}}$  and  $\text{Cu}_{\text{i}}$  shallow states as depicted in Figure 9b.

Now, one may be inclined to suggest that the maximum at 546 nm (2.27 eV) shown in Figure 3 is related to the indirect transition that may occur between the  $\Gamma$  conduction band minimum and R valence band maximum as shown in Figure 8. However, the maximum at 503 nm (2.46 eV) in Figure 3 is not close to any of the direct or indirect transitions determined by DFT. The M–X and/or R–M indirect transitions, both of which have energies of 2.83 eV, are the only closest ones to the peak at 503 nm (2.46 eV) in Figure 3.

Alternatively, the duo of maxima at 546 (2.27 eV) and 503 nm (2.46 eV) might be related to the M and R direct energy band gaps of specific regions of  $\text{Cu}_3\text{N}$  having a different lattice constant and larger, direct energy band gaps due to strain. As it is evident from Figure 2d, the M and R direct energy band gaps of  $\text{Cu}_3\text{N}$  are strongly dependent on strain and change from 1.89 to 2.12 eV and 1.93 to 2.08 eV, respectively, under a 2% hydrostatic strain that changes the lattice constant from 3.826 to 3.903 Å. In contrast, Birkett et al.<sup>57</sup> showed that the direct band gap changes from 1.4 up to 2.0 eV and the indirect gap from 0.6 up to 1.8 eV upon increasing the lattice from 3.8 to 3.9 Å. Evidently, the energy band gap of  $\text{Cu}_3\text{N}$  is strongly dependent on structural distortions and strain that may occur

under specific growth and annealing conditions. We have shown that the (100) XRD peak of  $\text{Cu}_3\text{N}$  in Figure 1a is shifted by  $2\theta = +0.4^\circ$  suggesting a strain of 2%. The duo of maxima at 546 (2.27 eV) and 503 nm (2.46 eV) are closer to the strained values of the direct energy band gaps, but a more accurate value of the strain, strain map, or uniformly strained layers are required in conjunction with theoretical calculations in order to quantify with higher precision the effect of strain on the energy band gaps of  $\text{Cu}_3\text{N}$ . Nevertheless, it is reasonable to suggest that certain crystalline domains or grains of  $\text{Cu}_3\text{N}$  might be subjected to varying extents of strain and distortion each having a different optical band gap. In fact, it is known that the surface oxidation of  $\text{Cu}_3\text{N}$  under ambient conditions results into such a strain.<sup>87</sup>

Now, the nonradiative recombination and decay of the carriers that occupy states in the M and R direct energy conduction bands of the bulk  $\text{Cu}_3\text{N}$  corresponding to the maxima at 627 (1.98 eV) and 662 nm (1.87 eV) appear to face a bottleneck and have longer lifetimes than the carriers occupying states related to the duo of maxima at 546 (2.27 eV) and 503 nm (2.46 eV). This is probably due to a higher density of defects, for example, inside the strained regions or at their grain boundaries, which however needs to be clarified both experimentally and theoretically in the future. On the other hand, one may observe in Figure 4f that the lifetime of the carriers in  $\text{Cu}_3\text{N}$  drops monotonically with increasing temperature. As already pointed out, we observed that a stronger interdiffusion occurs between the Cu and underlying f-SiO<sub>2</sub> with increasing temperature. This is expected to generate a higher density of defects at the grain boundaries of crystalline regions of  $\text{Cu}_3\text{N}$  resulting in even faster carrier recombination and a reduction of the carrier lifetime. In other words, the f-SiO<sub>2</sub> influences the properties of the  $\text{Cu}_3\text{N}$  layer as the annealing temperature is increased, so the choice of substrate or buffer layers must be considered carefully in optimizing the properties of  $\text{Cu}_3\text{N}$  layers for devices.

Finally, it is worthwhile pointing out that the higher-energy maxima at 546 (2.27 eV) and 503 nm (2.46 eV) shown in Figure 3 are not likely related to the formation of  $\text{Cu}_3\text{N}$  nanostructures and quantization as in this case we would expect to observe PL similar to Sithole et al.,<sup>88</sup> who found that  $\text{Cu}_3\text{N}$  nanoparticles exhibited PL at  $\lambda = 550 \text{ nm}$  ( $\approx 2.5 \text{ eV}$ ) due to quantum confinement, and Rahmati et al.,<sup>89</sup> who also observed PL from nanocrystalline Ti: $\text{Cu}_3\text{N}$  at  $\lambda = 375$  and 701 nm. Similarly, Strozecka et al.<sup>90</sup> observed electroluminescence at 1.5 and 2.0 eV from  $\text{Cu}_3\text{N}$  nanocrystals embedded in Cu (110) that were prepared by extended sputtering under  $\text{N}^+$ . They suggested that the  $\text{Cu}_3\text{N}$  nanocrystals behave as quantum electron boxes that are capable of light emission. The spectral analysis of the emitted light revealed multiple luminescence channels that operate in parallel and that most of the light comes from direct-inelastic transitions of tunneling electrons decaying into the nanocrystal states. Hence, despite the fact that  $\text{Cu}_3\text{N}$  is an indirect band gap semiconductor, it appears to be capable of light emission if it occurs in the form of nanostructures. However, we did not observe any PL from the  $\text{Cu}_3\text{N}$  between 77 and 300 K, and quantization would require confinement by a barrier. It has been shown by Modin et al.<sup>91</sup> that  $\text{Cu}_3\text{N}$  containing an excess of Cu atoms, O<sub>2</sub> impurities, and N vacancies has a tendency to form Cu-rich areas that will surround  $\text{Cu}_3\text{N}$ . Considering that the work function of  $\text{Cu}_3\text{N}$  is  $\sim 0.9 \text{ eV}$  larger than that of Cu<sup>92</sup> and that  $\text{Cu}_3\text{N}$  has a work function of 5.04 eV,<sup>93</sup> we expect that the Cu/ $\text{Cu}_3\text{N}$  metal–

semiconductor interface will not lead to quantum confinement in  $\text{Cu}_3\text{N}$  as shown Figure 10a. Similarly, the oxidation of  $\text{Cu}_3\text{N}$

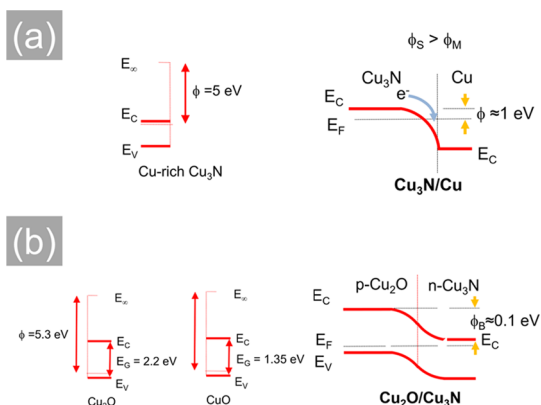


**Figure 10.** (a) Schematic energy band diagram of n-type Cu-rich  $\text{Cu}_3\text{N}$  showing the work function  $\phi$  and band profile of the Cu/ $\text{Cu}_3\text{N}$  metal–semiconductor contact; (b) energy band gap and work functions of p-type  $\text{CuO}$  and  $\text{Cu}_2\text{O}$ ; also shown is the band profile of a  $\text{Cu}_2\text{O}/\text{Cu}_3\text{N}$  p–n heterojunction.

and the formation of  $\text{Cu}_3\text{N}/\text{Cu}_2\text{O}$  and  $\text{Cu}_3\text{N}/\text{CuO}$  p–n heterojunctions will have small barriers and will not result in strong confinement as shown in Figure 10b. Therefore, it is unlikely that the spectral structure and maxima at 546 (2.27 eV) and 503 nm (2.46 eV) shown in Figure 3 are due to quantum confinement. From the discussion above, one may suggest that the overall absorption of a device consisting of multiple layers of  $\text{Cu}_3\text{N}$  with different degrees of strain would inherently absorb photons more effectively across the visible region due to the fact that the direct energy band gaps would change in each layer, consistent with theoretical results on the variation of the band gap with the lattice constant. We ought to mention in closing that the maxima observed by UPPS match very well with the energies extracted from an analysis of the steady-state UV–vis spectra shown in Figure 2. However, UPPS can be used as an effective tool for understanding even more about  $\text{Cu}_3\text{N}$  at a fundamental level, for example, finding how the direct energy band gap changes with strain, reduced dimensionality and size, and lifetimes, which in turn will provide deeper insight in conjunction with theoretical calculations as to how this novel material may be used for the realization of solar cells.

#### 4. CONCLUSIONS

We have grown  $\text{Cu}_3\text{N}$  from Cu under a flow of  $\text{NH}_3:\text{O}_2$  between 400 and 600 °C. The  $\text{Cu}_3\text{N}$  has a cubic crystal structure and exhibited maxima in differential transmission measured by UPPS at  $\sim 500$ , 550, and 630, 670 nm with the same spectral structure and shape on a fs time scale. Our primary conclusion is that the maxima in transmission at  $\sim 630$ , 670 nm are related to the M and R direct energy bands of unstrained regions of  $\text{Cu}_3\text{N}$ , in excellent agreement with DFT theory calculations. The observation of the M and R direct band gaps of  $\text{Cu}_3\text{N}$  by UPPS in essence confirms that it is a defect-tolerant semiconductor with defect states that are energetically located very close to the conduction and valence bands. Consequently, UPPS can be used as an effective tool not only for understanding  $\text{Cu}_3\text{N}$  at a fundamental level but also for the characterization of solar cells. These findings are corroborated by the fact that  $\text{Cu}_3\text{N}$  obtained by sputtering

under 100%  $\text{N}_2$  at  $10^{-2}$  mbar exhibited poor crystallinity and no spectral structure by UPPS due to a smeared density of states and large density of defects, but annealing under  $\text{NH}_3:\text{H}_2$  between 300 and 400 °C resulted in the same spectral response as that of  $\text{Cu}_3\text{N}$  obtained from Cu under  $\text{NH}_3:\text{O}_2$ .

In addition to our primary conclusion, we suggest that the maxima at 500 and 550 nm might be related to domains of  $\text{Cu}_3\text{N}$  under strain having a higher density of defects due to surface oxidation and/or the out-diffusion of oxygen from the underlying f- $\text{SiO}_2$ . The preparation of uniformly strained  $\text{Cu}_3\text{N}$  layers and theoretical calculations concerning the out-diffusion, reaction and incorporation of oxygen are required to clarify the effect of strain on the energy band gaps.

#### AUTHOR INFORMATION

##### Corresponding Author

**Matthew Zervos** – Nanostructured Materials and Devices Laboratory, School of Engineering, University of Cyprus, Nicosia 1678, Cyprus; [orcid.org/0000-0002-6321-233X](https://orcid.org/0000-0002-6321-233X); Email: [zervos@ucy.ac.cy](mailto:zervos@ucy.ac.cy)

##### Authors

**Andreas Othonos** – Laboratory of Ultrafast Science, Department of Physics, University of Cyprus, Nicosia 1678, Cyprus  
**Marios Sergides** – Laboratory of Ultrafast Science, Department of Physics, University of Cyprus, Nicosia 1678, Cyprus  
**Theodore Pavloudis** – Department of Physics, Aristotle University of Thessaloniki, 54124 Thessaloniki, Greece  
**Joseph Kioseoglou** – Department of Physics, Aristotle University of Thessaloniki, 54124 Thessaloniki, Greece; [orcid.org/0000-0002-6933-2674](https://orcid.org/0000-0002-6933-2674)

Complete contact information is available at: <https://pubs.acs.org/10.1021/acs.jpcc.9b10303>

##### Notes

The authors declare no competing financial interest.

#### ACKNOWLEDGMENTS

This research is co-financed by Greece and the European Union (European Social Fund-ESF) through the Operational Programme “Human Resources Development, Education and Lifelong Learning” in the context of the project “Reinforcement of Postdoctoral Researchers - 2nd Cycle” (MIS-5033021), implemented by the State Scholarships Foundation (IKY). This work was supported by computational time granted from the National Infrastructures for Research and Technology S.A. (GRNET) in the National HPC facility - ARIS - under the project AIMONACA (PR008002).

#### REFERENCES

- (1) Jiang, A.; Qi, M.; Xiao, J. Preparation, Structure, Properties, and Application of Copper Nitride ( $\text{Cu}_3\text{N}$ ) Thin Films: A Review. *J. Mater. Sci. Technol.* **2018**, *34*, 1467–1473.
- (2) Fioretti, A. N.; Pan, J.; Ortiz, B. R.; Melamed, C. L.; Dipppo, P. C.; Schelhas, L. T.; Perkins, J. D.; Kuciauskas, D.; Lany, S.; Zakutayev, A.; Toberer, E. S.; Tamboli, A. C. Exciton Photoluminescence and Benign Defect Complex Formation in Zinc Tin Nitride. *Mater. Horiz.* **2018**, *5*, 823–830.
- (3) Othonos, A.; Zervos, M. Carrier Relaxation Dynamics in  $\text{Sn}_x\text{N}_y$  Nanowires Grown by Chemical Vapor Deposition. *J. Appl. Phys.* **2009**, *106*, 114303.



- (4) Juza, R.; Hahn, H. Über die Kristallstrukturen von  $\text{Cu}_3\text{N}$ , GaN und InN Metallamide und Metallnitride. *Z. Anorg. Allg. Chem.* **1938**, 239, 282–287.
- (5) Zakutayev, A.; Caskey, C. M.; Fioretti, A. N.; Ginley, D. S.; Vidal, J.; Stevanovic, V.; Tea, E.; Lany, S. Defect Tolerant Semiconductors for Solar Energy Conversion. *J. Phys. Chem. Lett.* **2014**, 5, 1117–1125.
- (6) Suwannatus, S.; Duangsawat, B.; Pakdee, U. Lithium Storage Performance of Copper Nitride Films Deposited by Reactive DC Magnetron Sputtering. *Mater. Today: Proc.* **2018**, 5, 15208–15212.
- (7) Tian, X.; Tang, H.; Luo, J.; Nan, H.; Shu, T.; Du, L.; Zeng, J.; Liao, S.; Adzic, R. R. High-Performance Core–Shell Catalyst with Nitride Nanoparticles as a Core: Well-Defined Titanium Copper Nitride Coated with an Atomic Pt Layer for the Oxygen Reduction Reaction. *ACS Catal.* **2017**, 7, 3810–3817.
- (8) Cremer, R.; Witthaut, M.; Neuschütz, D.; Trappe, C.; Laurenzis, M.; Winkler, O.; Kurz, H. Deposition and Characterization of Metastable  $\text{Cu}_3\text{N}$  Layers for Applications in Optical Data Storage. *Microchim. Acta* **2000**, 133, 299–302.
- (9) Maruyama, T.; Morishita, T. Copper Nitride and Tin Nitride Thin Films for Write-Once Optical Recording Media. *Appl. Phys. Lett.* **1996**, 69, 890–891.
- (10) Lu, Q.; Zhang, X.; Zhu, W.; Zhou, Y.; Zhou, Q.; Liu, L.; Wu, X. Reproducible Resistive-Switching Behavior in Copper-Nitride Thin Film Prepared by Plasma-Immersion Ion Implantation. *Phys. Status Solidi A* **2011**, 208, 874–877.
- (11) Zhu, W.; Zhang, X.; Fu, X.; Zhou, Y.; Luo, S.; Wu, X. Resistive-Switching Behavior and Mechanism in Copper-Nitride Thin Films Prepared by DC Magnetron Sputtering. *Phys. Status Solidi A* **2012**, 209, 1996–2001.
- (12) Wang, Z.; Cao, X.; Liu, D.; Hao, S.; Kong, R.; Du, G.; Asiri, A. M.; Sun, X. Copper-Nitride Nanowires Array: An Efficient Dual-Functional Catalyst Electrode for Sensitive and Selective Non-Enzymatic Glucose and Hydrogen Peroxide Sensing. *Chem. – Eur. J.* **2017**, 23, 4986–4989.
- (13) Maruyama, T.; Morishita, T. Copper Nitride Thin Films Prepared by Radio-Frequency Reactive Sputtering. *J. Appl. Phys.* **1995**, 78, 4104–4107.
- (14) Yue, G. H.; Yan, P. X.; Liu, J. Z.; Wang, M. X.; Li, M.; Yuan, X. M. Copper Nitride Thin Film Prepared by Reactive Radio-Frequency Magnetron Sputtering. *J. Appl. Phys.* **2005**, 98, 103506.
- (15) Li, Z.; Li, X.; Zou, A.; Yuan, Z.; Yang, J.; Yao, K. Effect of  $\text{N}_2$ -Gas Partial Pressure on the Structure and Properties of Copper Nitride Films by DC Reactive Magnetron Sputtering. *Plasma Sci. Technol.* **2007**, 9, 147–151.
- (16) Wang, J.; Chen, J. T.; Miao, B. B.; Zhang, F.; Yan, P. X. The Effect of Hydrogen on  $\text{Cu}_3\text{N}$  Thin Films Deposited by Radio Frequency Magnetron Sputtering. *J. Appl. Phys.* **2006**, 100, 103509.
- (17) Li, X.; Liu, Z.; Zuo, A.; Yuan, Z.; Yang, J.; Yao, K. Properties of Al-Doped Copper Nitride Films Prepared by Reactive Magnetron Sputtering. *J. Wuhan Univ. Technol.-Mater. Sci. Ed.* **2007**, 22, 446–449.
- (18) Reddy, K. V. S.; Reddy, A. S.; Reddy, P. S.; Uthanna, S. Copper Nitride Films Deposited by DC Reactive Magnetron Sputtering. *J. Mater. Sci.: Mater. Electron.* **2007**, 18, 1003–1008.
- (19) Pierson, J. F. Structure and Properties of Copper Nitride Films Formed by Reactive Magnetron Sputtering. *Vacuum* **2002**, 66, 59–64.
- (20) Hadian, F.; Rahmati, A.; Movla, H.; Khaksar, M. Reactive DC Magnetron Sputter Deposited Copper Nitride Nano-Crystalline Thin Films: Growth and Characterization. *Vacuum* **2012**, 86, 1067–1072.
- (21) Li, X.; Bai, Q.; Yang, J.; Li, Y.; Wang, L.; Wang, H.; Ren, S.; Liu, S.; Huang, W. Effect of  $\text{N}_2$ -Gas Flow Rates on the Structures and Properties of Copper Nitride Films Prepared by Reactive DC magnetron Sputtering. *Vacuum* **2013**, 89, 78–81.
- (22) Yuan, X. M.; Yan, P. X.; Liu, J. Z. Preparation and Characterization of Copper Nitride Films at Various Nitrogen Contents by Reactive Radio-Frequency Magnetron Sputtering. *Mater. Lett.* **2006**, 60, 1809–1812.
- (23) Kim, K. J.; Kim, J. H.; Kang, J. H. Structural and Optical Characterization of  $\text{Cu}_3\text{N}$  Films Prepared by Reactive RF Magnetron Sputtering. *J. Cryst. Growth* **2001**, 222, 767–772.
- (24) Ghosh, S.; Singh, F.; Choudhary, D.; Avasthi, D. K.; Ganesan, V.; Shah, P.; Gupta, A. Effect of Substrate Temperature on the Physical Properties of Copper Nitride Films by R.F. Reactive Sputtering. *Surf. Coat. Technol.* **2001**, 142–144, 1034–1039.
- (25) Nowakowska-Langier, K.; Chodun, R.; Minikayev, R.; Okrasa, S.; Strzelecki, G. W.; Wicher, B.; Zdunek, K. Copper Nitride Layers Synthesized by Pulsed Magnetron Sputtering. *Thin Solid Films* **2018**, 645, 32–37.
- (26) Fan, X. Y.; Wu, Z. G.; Zhang, G. A.; Li, C.; Geng, B. S.; Li, H. J.; Yan, P. X. Ti-Doped Copper Nitride Films Deposited by Cylindrical Magnetron Sputtering. *J. Alloys Compd.* **2007**, 440, 254–258.
- (27) Wang, T.; Pan, X. J.; Wang, X. M.; Duan, H. G.; Li, R. S.; Li, H.; Xie, E. Q. Field Emission Property of Copper Nitride Thin Film Deposited by Reactive Magnetron Sputtering. *Appl. Surf. Sci.* **2008**, 254, 6817–6819.
- (28) Odeh, I. M. Fabrication and Optical Constants of Amorphous Copper Nitride Thin Films Prepared by Ion Beam Assisted DC Magnetron Reactive Sputtering. *J. Alloys Compd.* **2008**, 454, 102–105.
- (29) Xiao, J.; Li, Y.; Jiang, A. Structure, Optical Property and Thermal Stability of Copper Nitride Films Prepared by Reactive Radio Frequency Magnetron Sputtering. *J. Mater. Sci. Technol.* **2011**, 27, 403–407.
- (30) Pierson, J. F.; Horwat, D. Addition of Silver in Copper Nitride Films Deposited by Reactive Magnetron Sputtering. *Scr. Mater.* **2008**, 58, 568–570.
- (31) Cho, S. Effect of Substrate Temperature on the Properties of Copper Nitride Thin Films Deposited by Reactive Magnetron Sputtering. *Curr. Appl. Phys.* **2012**, 12, S44–S47.
- (32) Gordillo, N.; Gonzalez-Arrabal, R.; Martin-Gonzalez, M. S.; Olivares, J.; Rivera, A.; Briones, F.; Agulló-López, F.; Boerma, D. O. DC Triode Sputtering Deposition and Characterization of N-Rich Copper Nitride Thin Films: Role of Chemical Composition. *J. Cryst. Growth* **2008**, 310, 4362–4367.
- (33) Ji, A. L.; Huang, R.; Du, Y.; Li, C. R.; Wang, Y. Q.; Cao, Z. X. Growth of Stoichiometric  $\text{Cu}_3\text{N}$  Thin Films by Reactive Magnetron Sputtering. *J. Cryst. Growth* **2006**, 295, 79–83.
- (34) Wang, J.; Chen, J. T.; Yuan, X. M.; Wu, Z. G.; Miao, B. B.; Yan, P. X. Copper Nitride ( $\text{Cu}_3\text{N}$ ) Thin Films Deposited by RF Magnetron Sputtering. *J. Cryst. Growth* **2006**, 286, 407–412.
- (35) Zhang, G.; Yan, P.; Wu, Z.; Wang, J.; Chen, J. The Effect of Hydrogen on Copper Nitride Thin Films Deposited by Magnetron Sputtering. *Appl. Surf. Sci.* **2008**, 254, 5012–5015.
- (36) Gordillo, N.; Gonzalez-Arrabal, R.; Rivera, A.; Munnik, F.; Agulló-López, F. Stopping Power Dependence of Nitrogen Sputtering Yields in Copper Nitride Films under Swift-Ion Irradiation: Exciton Model Approach. *Nucl. Instrum. Methods Phys. Res., Sect. B* **2012**, 289, 74–78.
- (37) Ji, Z.; Zhang, Y.; Yuan, Y.; Wang, C. Reactive DC Magnetron Deposition of Copper Nitride Films for Write-Once Optical Recording. *Mater. Lett.* **2006**, 60, 3758–3760.
- (38) Matsuzaki, K.; Okazaki, T.; Lee, Y. S.; Hosono, H.; Susaki, T. Controlled Bipolar Doping in  $\text{Cu}_3\text{N}$  (100) Thin Films. *Appl. Phys. Lett.* **2014**, 105, 222102.
- (39) Li, Z.; Gordon, R. G. Thin, Continuous, and Conformal Copper Films by Reduction of Atomic Layer Deposited Copper Nitride. *Chem. Vap. Deposition* **2006**, 12, 435–441.
- (40) Park, J. M.; Jin, K.; Han, B.; Kim, M. J.; Jung, J.; Kim, J. J.; Lee, W. J. Atomic Layer Deposition of Copper Nitride Film and its Application to Copper Seed Layer for Electrodeposition. *Thin Solid Films* **2014**, 556, 434–439.
- (41) Gallardo-Vega, C.; de la Cruz, W. Study of the Structure and Electrical Properties of the Copper Nitride Thin Films Deposited by Pulsed Laser Deposition. *Appl. Surf. Sci.* **2006**, 252, 8001–8004.

- (42) Soto, G.; Díaz, J. A.; de la Cruz, W. Copper Nitride Films Produced by Reactive Pulsed Laser Deposition. *Mater. Lett.* **2003**, *57*, 4130–4133.
- (43) Matsuzaki, K.; Harada, K.; Kumagai, Y.; Koshiya, S.; Kimoto, K.; Ueda, S.; Sasase, M.; Maeda, A.; Susaki, T.; Kitano, M.; et al. High-Mobility p-Type and n-Type Copper Nitride Semiconductors by Direct Nitriding Synthesis and In Silico Doping Design. *Adv. Mater.* **2018**, *30*, 1801968.
- (44) Zakutayev, A. Design of Nitride Semiconductors for Solar Energy Conversion. *J. Mater. Chem. A* **2016**, *4*, 6742.
- (45) Du, Y.; Ji, A. L.; Ma, L. B.; Wang, Y. Q.; Cao, Z. X. Electrical Conductivity and Photorefectance of Nanocrystalline Copper Nitride Thin Films Deposited at Low Temperature. *J. Cryst. Growth* **2005**, *280*, 490–494.
- (46) Gao, L.; Ji, A. L.; Zhang, W. B.; Cao, Z. X. Insertion of Zn Atoms into  $\text{Cu}_3\text{N}$  Lattice: Structural Distortion and Modification of Electronic Properties. *J. Cryst. Growth* **2011**, *321*, 157–161.
- (47) Du, X.; Zhou, Q.; Yan, Z.; Zhou, Y. N.; Wu, X. The Effects of Oxygen Plasma Implantation on Bipolar Resistive-Switching Properties of Copper Nitride Thin Films. *Thin Solid Films* **2017**, *625*, 100–105.
- (48) Du, Y.; Huang, R.; Song, R.; Ma, L. B.; Liu, C.; Li, C. R.; Cao, Z. X. Effect of Oxygen Inclusion on Microstructure and Thermal Stability of Copper Nitride Thin Films. *J. Mater. Res.* **2007**, *22*, 3052–3057.
- (49) Lindahl, E.; Ottosson, M.; Carlsson, J. O. Doping of Metastable  $\text{Cu}_3\text{N}$  at Different Ni Concentrations: Growth, Crystallographic Sites and Resistivity. *Thin Solid Films* **2018**, *647*, 1–8.
- (50) Yu, A.; Hu, R.; Liu, W.; Zhang, R.; Zhang, J.; Pu, Y.; Chu, L.; Yang, J.; Li, X. Preparation and Characterization of Mn Doped Copper Nitride Films with High Photocurrent Response. *Curr. Appl. Phys.* **2018**, *18*, 1306–1312.
- (51) Yu, A.; Ma, Y.; Chen, A.; Li, Y.; Zhou, Y.; Wang, Z.; Zhang, J.; Chu, L.; Yang, J.; et al. Thermal Stability and Optical Properties of Sc-Doped Copper Nitride Films. *Vacuum* **2017**, *141*, 243–248.
- (52) Hayashi, Y.; Ishikawa, T.; Shimokawa, D. Modification of Electrical and Optical Properties of Metal Nitride Thin films by Hydrogen Inclusion. *J. Alloys Compd.* **2002**, *330–332*, 348–351.
- (53) Sahoo, G.; Meher, S. R.; Jain, M. K. Room Temperature Growth of High Crystalline Quality  $\text{Cu}_3\text{N}$  Thin Films by Modified Activated Reactive Evaporation. *Mater. Sci. Eng., B* **2015**, *191*, 7–14.
- (54) Dorrani, D.; Dejam, L.; Sari, A. H.; Hojabri, A. Effect of Nitrogen Content on Optical Constants of Copper Nitride Thin Films Prepared by DC Magnetron Reactive Sputtering. *J. Theor. Appl. Phys.* **2009**, *3*, 37–41.
- (55) Gonzalez-Arrabal, R.; Gordillo, N.; Martin-Gonzalez, M. S.; Ruiz-Bustos, R.; Agulló-López, F. Thermal Stability of Copper Nitride Thin Films: The Role of Nitrogen Migration. *J. Appl. Phys.* **2010**, *107*, 103513.
- (56) Borsa, D. M.; Boerma, D. O. Growth, Structural and Optical Properties of  $\text{Cu}_3\text{N}$  Films. *Surf. Sci.* **2004**, *548*, 95–105.
- (57) Birkett, M.; Savory, C. N.; Fioretti, A. N.; Thompson, P.; Muryn, C. A.; Weerakkody, A. D.; Mitrovic, I. Z.; Hall, S.; Treharne, R.; Dhanak, V. R.; Scanlon, D. O.; Zakutayev, A.; Veal, T. D. Atypically Small Temperature-Dependence of the Direct Band Gap in the Metastable Semiconductor Copper Nitride  $\text{Cu}_3\text{N}$ . *Phys. Rev. B* **2017**, *95*, 115201.
- (58) Yee, Y. S.; Inoue, H.; Hultqvist, A.; Hanifi, D.; Salleo, A.; Magyari-Köpe, B.; Nishi, Y.; Bent, S. F.; Clemens, B. M. Copper Interstitial Recombination Centers in  $\text{Cu}_3\text{N}$ . *Phys. Rev. B* **2018**, *97*, 245201.
- (59) Othonos, A.; Zervos, M.; Pervolaraki, M. Ultrafast Carrier Relaxation in InN Nanowires Grown by Reactive Vapor Transport. *Nanoscale Res. Lett.* **2009**, *4*, 122–129.
- (60) Born, B.; Krupa, J. D. A.; Geoffroy-Gagnon, S.; Hristovski, I. R.; Collier, C. M.; Holzman, J. F. Ultrafast Charge Carrier Dynamics of Copper Oxide Nanocrystals. *ACS Photonics* **2016**, *3*, 2475–2481.
- (61) Platzman, I.; Brener, R.; Haick, H.; Tannenbaum, R. Oxidation of Polycrystalline Copper Thin Films at Ambient Conditions. *J. Phys. Chem. C* **2008**, *112*, 1101–1108.
- (62) Rha, S. K.; Lee, W. J.; Lee, S. Y.; Kim, D. W.; Park, C. O.; Chun, S. S. Effects of the Annealing in Ar and  $\text{H}_2/\text{Ar}$  Ambients on the Microstructure and the Electrical Resistivity of the Copper Film Prepared by Chemical Vapor Deposition. *Jpn. J. Appl. Phys.* **1996**, *35*, 5781.
- (63) Lee, H.; Chakrabarti, K.; Lee, C. Effects of Post-Deposition Annealing on the Copper Films Electrodeposited on the ECR Plasma Cleaned Copper Seed Layer. *Jpn. J. Appl. Phys.* **2002**, *41*, 7476.
- (64) Othonos, A.; Zervos, M.; Christofides, C. A Systematic Investigation into the Conversion of  $\beta\text{-Ga}_2\text{O}_3$  to GaN Nanowires using  $\text{NH}_3$  and  $\text{H}_2$ : Effects on the Photoluminescence Properties. *J. Appl. Phys.* **2010**, *108*, 124319.
- (65) Kresse, G.; Furthmüller, J. Efficiency of Ab-Initio Total Energy Calculations for Metals and Semiconductors Using a Plane-Wave Basis Set. *Comput. Mater. Sci.* **1996**, *6*, 15–50.
- (66) Kresse, G.; Furthmüller, J. Efficient Iterative Schemes for Ab Initio Total-Energy Calculations Using a Plane-Wave Basis Set. *Phys. Rev. B* **1996**, *54*, 11169.
- (67) Blöchl, P. E. Projector Augmented-Wave Method. *Phys. Rev. B* **1994**, *50*, 17953.
- (68) Kresse, G.; Joubert, D. From ultrasoft pseudopotentials to the projector augmented-wave method. *Phys. Rev. B* **1999**, *59*, 1758–1775.
- (69) Perdew, J. P.; Burke, K.; Ernzerhof, M. Generalized Gradient Approximation Made Simple. *Phys. Rev. Lett.* **1996**, *77*, 3865–3868.
- (70) Perdew, J. P.; Burke, K.; Ernzerhof, M. Generalized Gradient Approximation Made Simple [Phys. Rev. Lett. *77*, 3865 (1996)]. *Phys. Rev. Lett.* **1997**, *78*, 1396.
- (71) Heyd, J.; Scuseria, G. E.; Ernzerhof, M. Hybrid functionals based on a screened Coulomb potential. *J. Chem. Phys.* **2003**, *118*, 8207–8215.
- (72) Heyd, J.; Scuseria, G. E. Efficient hybrid density functional calculations in solids: Assessment of the Heyd–Scuseria–Ernzerhof screened Coulomb hybrid functional. *J. Chem. Phys.* **2004**, *121*, 1187–1192.
- (73) Heyd, J.; Scuseria, G. E.; Ernzerhof, M. Erratum: “Hybrid functionals based on a screened Coulomb potential” [J. Chem. Phys. *118*, 8207 (2003)]. *J. Chem. Phys.* **2006**, *124*, 219906.
- (74) Krukau, A. V.; Vydrov, O. A.; Izmaylov, A. F.; Scuseria, G. E. Influence of the exchange screening parameter on the performance of screened hybrid functionals. *J. Chem. Phys.* **2006**, *125*, 224106.
- (75) Wang, L.; Maxisch, T.; Ceder, G. Oxidation energies of transition metal oxides within the GGA+U framework. *Phys. Rev. B* **2006**, *73*, 195107.
- (76) Jain, A.; Hautier, G.; Ong, S. P.; Moore, C. J.; Fischer, C. C.; Persson, K. A.; Ceder, G. Formation enthalpies by mixing GGA and GGA + U calculations. *Phys. Rev. B* **2011**, *84*, No. 045115.
- (77) Dudarev, S. L.; Botton, G. A.; Savrasov, S. Y.; Humphreys, C. J.; Sutton, A. P. Electron-energy-loss spectra and the structural stability of nickel oxide: An LSDA+U study. *Phys. Rev. B* **1998**, *57*, 1505–1509.
- (78) Suleiman, M. S. H.; Molepo, M. P.; Joubert, D. P. A theoretical investigation of structural, electronic and optical properties of bulk copper nitrides. *J. Alloys Compd.* **2018**, *753*, 576–585.
- (79) Winiarski, M. J. Band gap evolution of bulk  $\text{Cu}_3\text{N}$  and monolayer  $\text{Cu}_2\text{N}$  under nonhydrostatic strain. *J. Solid State Chem.* **2018**, *266*, 161–165.
- (80) Zhao, Y.; Zhang, Q.; Huang, S.; Zhang, J.; Ren, S.; Wang, H.; Wang, L.; Yang, T.; Yang, J.; Li, X. a. Effect of magnetic transition metal (TM = V, Cr, and Mn) dopant on characteristics of copper nitride. *J. Supercond. Novel Magn.* **2016**, *29*, 2351–2357.
- (81) Yan, Q.; Rinke, P.; Scheffler, M.; Van de Walle, C. G. Strain effects in group-III nitrides: Deformation potentials for AlN, GaN, and InN. *Appl. Phys. Lett.* **2009**, *95*, 121111.

- (82) Pavloudis, T.; Kioseoglou, J.; Karakostas, T.; Komninou, P. Ordered Structures in III-Nitride Ternary Alloys. *Comput. Mater. Sci.* **2016**, *118*, 22–31.
- (83) Nolan, M.; Elliott, S. D. The p-type Conduction Mechanism in  $\text{Cu}_2\text{O}$ : a First Principles Study. *Phys. Chem. Chem. Phys.* **2006**, *8*, 5350–5358.
- (84) Chen, H.; Li, X.; Zhao, J.; Wu, Z.; Yang, T.; Ma, Y.; Huang, W.; Yao, K. First Principles Study of Anti- $\text{ReO}_3$  Type  $\text{Cu}_3\text{N}$  and Sc-Doped  $\text{Cu}_3\text{N}$  on Structural, Elastic and Electronic Properties. *Comput. Theor. Chem.* **2013**, *1018*, 71–76.
- (85) Kong, F.; Hu, Y.; Wang, Y.; Wang, B.; Tang, L. Structural, Elastic and Thermodynamic Properties of Anti- $\text{ReO}_3$  Type  $\text{Cu}_3\text{N}$  under Pressure From First Principles. *Comput. Mater. Sci.* **2012**, *65*, 247–253.
- (86) Moreno-Armenta, M. G.; Martínez-Ruiz, A.; Takeuchi, N. Ab Initio Total Energy Calculations of Copper Nitride: the Effect of Lattice Parameters and Cu Content in the Electronic Properties. *Solid State Sci.* **2004**, *6*, 9–14.
- (87) Majumdar, A.; Drache, S.; Wulff, H.; Mukhopadhyay, A. K.; Bhattacharyya, S.; Helm, C. A.; Hippler, R. Strain Effects by Surface Oxidation of  $\text{Cu}_3\text{N}$  Thin Films Deposited by DC Magnetron Sputtering. *Coatings* **2017**, *7*, 64.
- (88) Sithole, R. K.; Machogo, L. F. E.; Airo, M. A.; Gqoba, S. S.; Moloto, M. J.; Shumbula, P.; van Wyk, J.; Moloto, N. Synthesis and Characterization of  $\text{Cu}_3\text{N}$  Nanoparticles Using Pyrrole-2-Carbaldehyde Pyridine  $\text{Cu}(\text{II})$  Complex and  $\text{Cu}(\text{NO}_3)_2$  as Single-Source Precursors: the Search For an Ideal Precursor. *New J. Chem.* **2018**, *42*, 3042.
- (89) Rahmati, A.; Bidadi, H.; Ahmadi, K.; Hadian, F. Ti Substituted Nano-Crystalline  $\text{Cu}_3\text{N}$  Thin Films. *J. Coat. Technol. Res.* **2011**, *8*, 289–297.
- (90) Stróżecka, A.; Li, J.; Schürmann, R.; Schulze, G.; Corso, M.; Schulz, F.; Lotze, C.; Sadewasser, S.; Franke, K. J.; Pascual, J. I. Electroluminescence of Copper-Nitride Nanocrystals. *Phys. Rev. B* **2014**, *90*, 195420.
- (91) Modin, A.; Kvashnina, K. O.; Butorin, S. M.; Werme, L.; Nordgren, J.; Arapan, S.; Ahuja, R.; Fallberg, A.; Ottosson, M. Electronic Structure of  $\text{Cu}_3\text{N}$  Films Studied by Soft x-Ray Spectroscopy. *J. Phys.: Condens. Matter* **2008**, *20*, 235212.
- (92) Bhattacharjee, K.; Ma, X. D.; Zhang, Y. Q.; Przybylski, M.; Kirschner, J. Electronic Structure of the Corrugated  $\text{Cu}_3\text{N}$  Network on Cu (110): Tunneling Spectroscopy Investigations. *Surf. Sci.* **2012**, *606*, 652–658.
- (93) Wang, L.-C.; Liu, B.-H.; Su, C.-Y.; Liu, W.-S.; Kei, C.-C.; Wang, K.-W.; Perng, T.-P. Electronic Band Structure and Electrocatalytic Performance of  $\text{Cu}_3\text{N}$  Nanocrystals. *ACS Appl. Nano Mater.* **2018**, *1*, 3673–3681.